

1 **Examining Parameterizations of Potential Temperature**  
2 **Variance Across Varied Landscapes for use in Earth**  
3 **System Models**

4 **T. Waterman<sup>1</sup>, A.D. Bragg<sup>1</sup>, G. Katul<sup>1</sup>, N. Chaney<sup>1</sup>**

5 <sup>1</sup>Department of Civil and Environmental Engineering, Duke University Pratt School of Engineering,  
6 Durham, NC USA

7 **Key Points:**

- 8 • Models of potential temperature variance in the surface layer based on similar-  
9 ity theory were evaluated using data from 39 varied sites
- 10 • Existing schemes perform well across most surfaces, although the data shows a  
11 significant bias in the values of the similarity constants
- 12 • Canopy structure and surface heterogeneity drive a large portion of inter-site vari-  
13 ability in model performance

---

Corresponding author: Tyler Waterman, [tyler.waterman@duke.edu](mailto:tyler.waterman@duke.edu)

**Abstract**

Earth system models (ESMs) and mesoscale models have come to employ increasingly complex parameterization schemes for the atmospheric boundary layer (ABL), requiring surface boundary conditions for numerous higher order turbulence statistics. Of particular interest is the potential temperature variance (PTV), which is used not only as a boundary condition itself but also to close boundary conditions of other statistics. The existing schemes in ESMs largely rely on the assumptions of Monin-Obukhov similarity theory (MOST), and are not necessarily applicable over complex and heterogeneous surfaces where large scale circulations and roughness sub-layer effects may cause deviations from MOST. The National Ecological Network (NEON) is used here to evaluate existing parameterizations for the surface boundary of PTV, note key deficiencies, and explore possible remedies. The results indicate that existing schemes are acceptable over a variety of surface conditions provided the analysis of a priori filters out low frequency variability not associated with turbulent time scales. There was, however, significant inter-site variability in observed similarity constants and a significant bias when compared to the textbook values of these parameters. Existing models displayed the poorest performance over heterogeneous sites, and rough landscapes. Attempts to use canopy structure and surface roughness characteristics to improve the results confirmed a relation between these variables and PTV, but failed to significantly improve the predictive power of the models. The results did not find strong evidence indicating that large scale circulations caused substantial deviations from textbook models, although additional analysis is required to assess their full impacts.

**Plain Language Summary**

Modern models of the lower atmosphere, which are used to analyze climate change and weather, resolve increasingly complex characteristics of the turbulence in the atmosphere. An estimate for the value of many of these characteristics at the land surface is required to set boundary conditions for these models. An important boundary condition is the variance of very small temperature fluctuations that occur in the atmosphere due to turbulence. Currently, model estimates for these values assume the surface is flat and its characteristics do not change in space, which doesn't represent many of the conditions we wish to model over the earth. In addition, existing studies tend to only analyze data from a small number of locations. We analyzed data from a network of 39 sites and found that the current estimates work fairly well across a large variety of conditions, but that there is a bias in the constants often used and there are notable differences over forests, complex surfaces, and heterogeneous terrain. There is a clear relationship between surface characteristics such as tree canopy height and performance of the model, however it was not clear enough to improve our ability to predict the surface boundary condition.

**1 Introduction**

The atmospheric boundary layer (ABL) plays a fundamental role in the climate system due to its significance in bridging land surface fluxes of heat and water vapor to convection and cloud formation (Siqueira et al., 2009; Huang & Margulis, 2010; Garratt, 1992). The ABL is characterized by the coexistence of mechanically and thermally generated turbulence, which regulate mixing and transport properties and exchanges between the land surface and the lower atmosphere. The variances of turbulent quantities are of particular interest due to their emerging role in state-of-the-science Earth System Models (ESMs) and numerical weather prediction. They have accordingly received attention in the literature, although most of these studies have focused on the velocity variances. Comparatively few examine the potential temperature variance (PTV) and those that do often focus on flat homogeneous terrain (Albertson et al., 1995; Asanuma & Brut-

64 saert, 1999; G. G. Katul & Hsieh, 1999; Mironov & Sullivan, 2016; van de Boer et al.,  
 65 2014; Maronga & Reuder, 2017; Otić et al., 2005; Antonia et al., 1981; D. Li et al., 2016;  
 66 Monji, 1973; Champagne et al., 1977; Kiely et al., 1996). Traditional boundary layer schemes  
 67 in ESMs employed first-order or 1.5-order closure schemes (Cohen et al., 2015; Lock et  
 68 al., 2000), although increasingly many higher order schemes that resolve PTV prognos-  
 69 tically throughout the ABL are now in use, such as the Cloud Layers Unified by Bino-  
 70 mials (CLUBB) scheme in the Community Earth System Model (CESM) and the En-  
 71 ergy Exascale Earth System Model (E3SM) (Larson, 2017), the Mellor-Yamada-Nakanishi-  
 72 Niino model (MYNN) implemented in the meso-scale Weather Research and Forecast-  
 73 ing model and the Model for Interdisciplinary Research on Climate (MIROC) (Nakanishi  
 74 & Niino, 2009), and the intermediately prognostic higher-order turbulence closure (IPHOC)  
 75 implemented in the Community Atmosphere Model, version 5 (Cheng & Xu, 2015). How-  
 76 ever, less attention has been placed on the surface boundary condition of PTV of these  
 77 schemes despite their use in the aforementioned models and the fact that many higher  
 78 order terms are closed based this temperature variance.

The specification of the lower boundary conditions in such schemes utilize Monin-  
 Obukhov Similarity Theory (MOST) that rests on the assumptions of stationary and planar  
 homogeneous, high Reynolds number flow in the absence of subsidence (Monin &  
 Obukhov, 1954). For these idealized conditions, the turbulent fluxes are assumed to be  
 invariant with distance from the boundary and all flow statistics can be reduced to a set  
 of universal curves that vary with the atmospheric stability parameter (Foken, 2006).  
 Currently, one of two parameterization schemes, both consistent with MOST (Tillman,  
 1972; J. Wyngaard & Coté, 1971) for unstable atmospheric conditions are used in ESMs  
 and are given by

$$\frac{\overline{\theta'^2}}{T_*^2} = a(1 - b\zeta)^{-2/3}, \quad (1)$$

and

$$\frac{\overline{\theta'^2}}{T_*^2} = C_1(-\zeta)^{-2/3}, \quad (2)$$

where  $\theta'$  is the fluctuating potential temperature, overline indicates time-averaging over  
 a period that is sufficiently long to reliably capture the ensemble statistics of turbulence  
 but short enough relative to variations in the mean state of the ABL,  $a$ ,  $b$ , and  $C_1$  are  
 similarity constants,  $\zeta$  is the atmospheric stability parameter defined as

$$\zeta = \frac{z - z_d}{L}, \quad (3)$$

with  $z_d$  being the zero-plane displacement height,  $z$  is the measurement height and  $L$  is  
 the Obukhov length (Obukhov, 1946) given by

$$L = -\frac{u_*^3 \overline{\theta_v}}{kgw'\overline{\theta'}}, \quad (4)$$

where  $k = 0.4$  is the von Kármán constant,  $g$  is the gravitational acceleration,  $u_*$  is the  
 friction velocity,  $\overline{\theta_v}$  is the mean virtual potential temperature,  $\overline{w'\theta'}$  is the kinematic tur-  
 bulent sensible heat flux, and  $w'$  is the turbulent vertical velocity. Unstable atmospheric  
 stability conditions is defined by  $\zeta < 0$  whereas near-neutral atmospheric stability con-  
 ditions occurs when  $|\zeta| < 0.05$ . The  $T_*$  is the non-dimensional temperature scale de-  
 fined as

$$T_* = \frac{\overline{w'\theta'}}{u_*}. \quad (5)$$

Equations (1) and (2) converge as near-convective conditions ( $-\zeta \gg 1$ ) are approached  
 resulting in  $ab^{-2/3} = C_1$ . For these conditions, the turbulent heat flux can be linked  
 to  $\sigma_T = \sqrt{\overline{\theta'^2}}$  through the well known flux-variance expression (Tillman, 1972)

$$\overline{w'\theta'} = C_1^{-3} [kg(z - z_d)]^{1/2} \overline{\theta_v}^{-1/2} \sigma_T^{3/2}. \quad (6)$$

79 This expression suggests that sensible heat only depends on  $\sigma_T$  and  $(z - z_d)$  indepen-  
 80 dent of  $u_*$  as expected when convective conditions are approached. For near neutral condi-  
 81 tions with  $u_* > 0$  and  $\zeta \rightarrow 0$ , equation (1) ensures  $\frac{\sigma_T}{T_*} \rightarrow \sqrt{a}$  whereas equation (2)  
 82 suggests that  $\sigma_T$  is indeterminate by MOST. The two-third scaling is fixed for the pur-  
 83 poses of this study - a reasonable assumption as it matches the logical, dimensional lim-  
 84 its of free convection.

85 The ‘textbook’ similarity constants estimated in the literature are  $a = 4, b = 8.3$ ,  
 86 and  $C_1 = 0.95$ . These values were initially derived from experiments over flat, homo-  
 87 geneous wheat stubble in Kansas and confirmed by other studies over similarly homo-  
 88 geneous and largely flat terrain (Tillman, 1972; J. Wyngaard & Coté, 1971; J. C. Wyn-  
 89 gaard & Coté, 1974; Andre et al., 1978; Albertson et al., 1995; Haugen et al., 1971; Monji,  
 90 1973). This lends some support to their supposed universal character. However, MOST  
 91 is not readily generalizable for application in ESMs over more realistic landscapes, tall  
 92 forests and a variety of atmospheric conditions such as those associated with significant  
 93 entrainment and mesoscale phenomenon (Kroon & de Bruin, 1995; Asanuma & Brut-  
 94 saert, 1999; Lloyd et al., 1991; Hang et al., 2018; Mcnaughton, 2006; van de Boer et al.,  
 95 2014; Wilson, 2008; Harman, 2012; Brunet, 2020; Q. Li et al., 2018). Previous literature  
 96 examining the scaling relation between  $\zeta$  and non-dimensional flow statistics has focused  
 97 on conditions that satisfy the assumptions of flat uniform surfaces so that the univer-  
 98 sal character suggested by MOST can be readily tested (Kader & Yaglom, 1990). How-  
 99 ever, comparatively less research has been carried out over non-idealized terrain. These  
 100 few studies have found that the MOST functions may not hold over surfaces such as sparse  
 101 and open canopies and heterogenous surfaces (Lee, 2009; Kroon & de Bruin, 1995; van de  
 102 Boer et al., 2014; Hang et al., 2018; Detto et al., 2008). Few studies have consistently  
 103 examined PTV across a wide variety of land cover types (G. Katul et al., 1995). The lat-  
 104 ter study suggested that local similarity may still hold (i.e. a local  $T_*$  and  $L$  can explain  
 105 the mathematical form of PTV) provided the similarity coefficients (e.g.  $C_1$ ) are allowed  
 106 to vary with land cover type. Despite these issues raised, the use of MOST scaling over  
 107 various landscapes is widespread in ESMs that require it (Nakanishi & Niino, 2009; Lar-  
 108 son, 2017; Zhao et al., 2018; Golaz et al., 2019, 2002; Cheng & Xu, 2015). To explore  
 109 PTV in the atmospheric surface layer across differing landscapes and a wide range of at-  
 110 mospheric conditions, observations covering many ecosystems and canopy structures with  
 111 appropriate parameterizations are becoming necessary and motivates the present work.

112 Since these parameterizations were developed, there has been a significant growth  
 113 in the availability of data across differing surfaces that can be used to re-examine MOST  
 114 parameterizations. One example is the National Ecological Observation Network (NEON).  
 115 NEON is a continent-scale network where high frequency (20 Hz) velocity and air tem-  
 116 perature fluctuations are sampled in a consistent manner (i.e. same instrumentation, rel-  
 117 ative heights, pre- and post-processing algorithms, etc..) over 39 sites that vary in cli-  
 118 mate and land-cover across the United States. Hence, the NEON high frequency data  
 119 set offers a unique opportunity to explore these similarity relations over many land cover  
 120 types (ideal and non-ideal) and  $\zeta$  conditions. Using this information, it is possible to ex-  
 121 plore validity and modifications to the traditional MOST PTV parameterizations. The  
 122 initial focus spans near-neutral to unstable stratification ( $\zeta < 0$ ), where the turbulence  
 123 is fully developed. Stably stratified conditions are characterized by a shallow boundary  
 124 layer depth and are infected with numerous non-turbulent phenomena that will require  
 125 a separate investigation that is better kept for a future study.

126 With this large data set, the time is ripe to revisit and reevaluate traditional schemes  
 127 for PTV in light of these contemporary needs of ESM. In doing so, the focus is on two  
 128 deviations from the assumptions of MOST. The first is mesoscale phenomenon and outer-  
 129 layer eddies that impinge onto the atmospheric surface layer, potentially introducing ad-  
 130 ditional length scales not captured by  $\zeta$ . The second is roughness sublayer effects, es-  
 131 pecially over forests or other forms of structured heterogeneity, which is not included as

132 part of MOST. This study seeks to quantify the significance of the distortions from both  
 133 mesoscale and roughness sublayer effects on equations (1) and (2), and examine if such  
 134 distortions can be partly absorbed in the parameters  $a$  and  $b$  (or  $C_1$ ). The approach that  
 135 follows takes advantage of the wealth of data provided by NEON as well as remotely sensed  
 136 sources, and the Random Forest (RF) method, which is a machine learning method able  
 137 to classify the significance of surrogate terms such as boundary layer height, land cover  
 138 type, canopy height, and other ancillary variables on  $\overline{\theta'^2}/T_*^2$ .

## 139 2 Data

140 The core turbulence data are publicly available from NEON and includes the tur-  
 141 bulance statistics, the bulk meteorological variables, as well as site specific information.  
 142 Additional information from remotely sensed datasets colocated with the NEON site data  
 143 are used in predictive models that seek to link environmental variables and land surface  
 144 features to PTV.

### 145 2.1 National Ecological Observation Network

146 The NEON sites are located within the continental United States (CONUS), Alaska,  
 147 Hawaii and Puerto Rico. Sites are centrally managed and designed, which means that  
 148 sampling and post-processing high frequency data are consistent, and differences can be  
 149 attributed to site characteristics rather than differences in management, methods and  
 150 instrumentation as is the case for other locally managed flux tower networks such as FLUXNET  
 151 or AmeriFlux (Novick et al., 2018). Moreover, the high frequency time series spanning  
 152 several years are publicly available thus enabling the determination of variances and heat  
 153 fluxes in a coherent manner when post-processed. Sites are also spread across different  
 154 ecological domains to ensure coverage of the different landscapes and ecosystems in North  
 155 America.

156 Each site includes a full suite of meteorological instrumentation, eddy covariance  
 157 measurements from a CSAT-3 sonic anemometer recording a 20 Hz and time averaged  
 158 to 30 min, and mean wind profiles throughout the canopy and above it, compiled into  
 159 one dataset (National Ecological Observatory Network (NEON), 2021). Towers at sites  
 160 with a canopy less than three meters are designed to be 8m tall, whereas towers at sites  
 161 with a canopy greater than three meters are designed to have a height corresponding to  
 162  $z_d + 4(h_c - z_d)$ , with canopy height  $h_c$ , to ensure that the turbulence exchange assem-  
 163 bly samples largely above the momentum roughness layer (Metzger et al., 2019). In ad-  
 164 dition, detailed canopy structure at each site is acquired through near-annual airborne  
 165 remote sensing surveys with discrete and full waveform LiDAR. Soil, vegetative and me-  
 166 teorological characteristics are described and continuously collected when appropriate  
 167 at each site. Only the 39 CONUS sites are included in this analysis.

168 For illustrative purposes, eight representative sites were selected as examples of site  
 169 level differences throughout the study. Wind River Experimental Forest (WREF) - a tall  
 170 evergreen forest in the Pacific Northwest, Northern Great Plains Research Laboratory  
 171 (NOGP) - a flat grassland site in North Dakota, Bartlett Experimental Forest (BART)  
 172 - a mixed deciduous evergreen forest in New England, Soaproot Saddle (SOAP) - a conifer  
 173 forest with complex terrain in the Sierra Nevada mountains, Oak Ridge National Lab  
 174 (ORNL) - a deciduous forest with some pine in Appalachia, Santa Rita Experimental  
 175 Range (SRER) - a semiarid scrub environment site in the Sonoran Desert, Konza Prairie  
 176 Biological Station (KONZ) - a pristine prairie site in Kansas, and Disney Wilderness Pre-  
 177 serve (DSNY) - a wetland site in the headwaters of the everglades.

**Table 1.** Summary table of the remotely sensed data and reanalysis products used in this project with their native spatial and temporal resolution as well as the source of the data

Variable	Spatial Resolution	Temporal Resolution	Source
$LAI$	250 m	8 days	MODIS
$f_{veg}$	250 m	1 year	MODIS
$f_{tree}$	250 m	1 year	MODIS
$f_{bare}$	250 m	1 year	MODIS
<i>Land Cover</i>	30 m	N/A	NLCD (Landsat)
$BLH$	30 km	1 hour	ERA 5 Reanalysis
$f_{cloud}$	30 km	1 hour	ERA 5 Reanalysis
$CAPE$	30 km	1 hour	ERA 5 Reanalysis

178

## 2.2 Remotely Sensed Datasets

179

180

181

One reanalysis product and three satellite remote sensing datasets are collocated with the NEON site data to complete a full coverage of vegetation, land cover, and meteorology at each site and summarized in Table 1.

182

183

184

185

186

187

188

189

190

191

192

Two MODIS derived satellite products are used including MODIS Leaf Area Index (LAI) (Myneni et al., 2015), which is reported at about 250m resolution every 8 days. The site is assigned the LAI of the grid cell in which the tower is contained, and linear interpolation is used to determine LAI for days in which MODIS LAI is unavailable. MODIS Vegetative Continuous Fields (VCF) (DiMiceli et al., 2015) includes measurements of vegetation cover at about 250m resolution on a yearly basis, with linear interpolation used to fill in gaps. Similar to MODIS LAI, MODIS VCF at each site for each point is assigned based on the VCF of the grid cell in which the tower is contained. The VCF product details low lying vegetation cover ( $f_{veg}$ ), tree cover ( $f_{tree}$ ), and bare soil coverage ( $f_{bare}$ ) percentages around each site. These products provide basic information about the vegetation structure.

193

194

195

196

The National Land Cover Dataset (NLCD), a Landsat derived product defining the land cover at 30m pixels over CONUS (Jin et al., 2019), is the third remote dataset employed. Fractional coverage of each landcover type within a 250m radius from the tower location is computed for each site, as well as the dominant NLCD land cover type.

197

198

199

200

201

ERA5 (Hersbach et al., 2018) is a reanalysis dataset that combines historical observations and modelling results to generate hourly data of a variety of land surface and atmospheric characteristics. For this analysis, the boundary layer height ( $BLH$ ), total cloud cover ( $f_{cloud}$ ) and Convective Available Potential Energy ( $CAPE$ ) are used to include the impacts on mesoscale phenomenon.

202

## 3 Methods

203

204

205

206

207

208

209

210

Turbulence statistics as directly acquired from NEON includes variance information from non-turbulence sources whereas models such as CLUBB focus on variances produced by turbulent eddies. A filtering process is required to remove non-turbulent events (and lack of stationarity) before they can be used for analysis. In addition, computed  $z_d$  is required for the tower area, as values reported by NEON are suspect and represent the physical characteristics of the entire ecological site rather than the local tower footprint. These values are needed to assess the influence of surface roughness on the development of turbulence. One method of analysis to be used is the Random Forest (RF)

211 method, which is employed to determine what physical and environmental characteris-  
 212 tics are most significant for the development of variance without constraints imposed by  
 213 similarity theory and concomitant dimensional analysis.

### 214 3.1 Filtering

215 One of the key assumptions for the MOST parameterizations is the stationarity of  
 216 the temperature time series. The data for the majority of atmospheric conditions at each  
 217 site are not strictly stationary. Any computed temperature variance value captures vari-  
 218 ance associated with turbulent eddies and meso-scale disturbances as well as non-stationarity  
 219 found at transitions from night to day and vice-a-versa. To fulfill the requirement of solely  
 220 including PTV caused by turbulence as required by ESMs, a high pass filter with a cut-  
 221 off time scale of 5 min is applied to the high frequency air temperature time series in the  
 222 Fourier domain. An example application of the high pass filter is featured in figure 1.  
 223 Time scales exceeding 5 minutes in the air temperature spectra are assumed to be not  
 224 associated with turbulent eddies produced by mechanical or buoyant production near  
 225 the surface. In fact, the choice of 5 minutes exceeds by at least one to two orders of mag-  
 226 nitude measured peaks in the co-spectra of  $w'$  and  $\theta'$  or the shear time scale  $k(z-z_d)/u_*$   
 227 linked with MOST. These events do not significantly impact turbulent sensible heat flux  
 228 but contribute appreciably to temperature variance. The remainder of the analysis pre-  
 229 sented herein uses the filtered temperature variance.

### 230 3.2 Canopy Structure Determination

While NEON does report site level  $h_c$  and  $z_d$ , both of which are needed for the anal-  
 ysis, these values appear to be reported as averages for the whole ecological site and not  
 the direct tower area, windshed, or source weight function. Reported  $z_d$  in particular ap-  
 pear to deviate significantly from experimentally derived values at a number of sites. As  
 such, the  $z_d$  is estimated here from measured mean wind profile data ( $u(z)$ ) assum-  
 ing a log wind profile and that  $u^*$  is approximately constant with  $z$  (as required by MOST).  
 We apply the following using the top three points in the mean wind profile under near-  
 neutral conditions so that the stability correction terms can be ignored (Oke, 1987)

$$\frac{du}{dz} = \frac{u_*}{k(z - z_d)}. \quad (7)$$

The resulting heights are seasonally averaged at each site and then interpolated for use  
 in the computation of  $\zeta$  via (4). The resulting  $z_d$ , seen in figure 2, follow the 2/3 rela-  
 tion reported in the literature (Garratt, 1992) over most sites. This relation, however,  
 is less clear at a number of sites with short vegetation. This deviation may not be sur-  
 prising. A basis for the  $z_d = (2/3)h_c$  relation stems from an exponential mean velocity  
 profile characterized by an extinction coefficient  $a_c > 1$  inside the canopy as derived  
 from a constant mixing length hypothesis for the turbulent eddy diffusivity. These ar-  
 guments, when combined with the drag-force centroid method to estimate  $z_d$  for (i) con-  
 stant drag coefficient and leaf area density and (ii) rigid, tall and dense canopy yield

$$\frac{z_d}{h_c} = 1 - \frac{1}{2a_c} = 1 - \frac{1}{2} \frac{L_s}{h_c}, \quad (8)$$

231 where  $L_s = u/(du/dz)$  evaluated at  $z = h_c$  is known as the canopy shear length scale.  
 232 For the flow near the canopy top to behave as 'mixing layers' requires an inflection point  
 233 in the mean velocity profile at  $z/h_c = 1$  (Raupach et al., 1996). This condition leads  
 234 to a constraint on  $1/2 < L_s/h_c < 1$  thereby bounding  $z_d/h_c$  to be between 1/2 and  
 235 3/4. All these assumptions (i.e. rigid, tall and dense canopy, constant mixing length within  
 236 the canopy, etc..) break down for short and sparse canopies (Poggi et al., 2004) as ev-  
 237 idenced by the near independence between  $z_d$  and  $h_c$  in Figure 2 for short  $h_c$ .

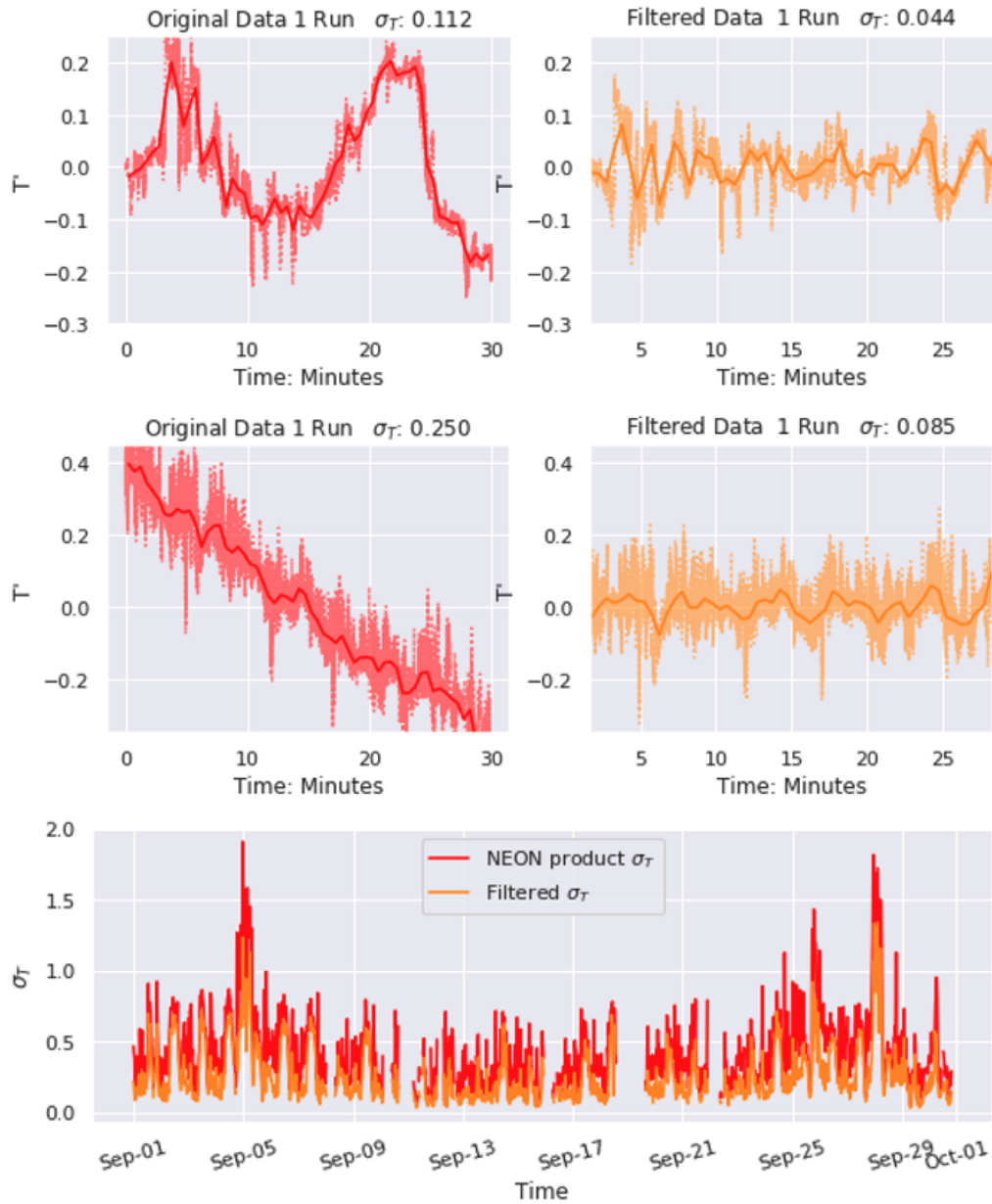


**Figure 1.** Illustration of filtering to reduce the effects of non-stationarity. Top row shows the raw unfiltered time series for one 30-minute run (left) and the same data after the high pass filter was employed where the nonlinear trend is removed (right). The second row shows the raw unfiltered data for another 30-minute run (left) and the same data after the high pass filter where the approximate linear trend is removed (right). The bottom plot illustrates the change in over a one-month period at the ABBY site from the unfiltered NEON product and the filtered data

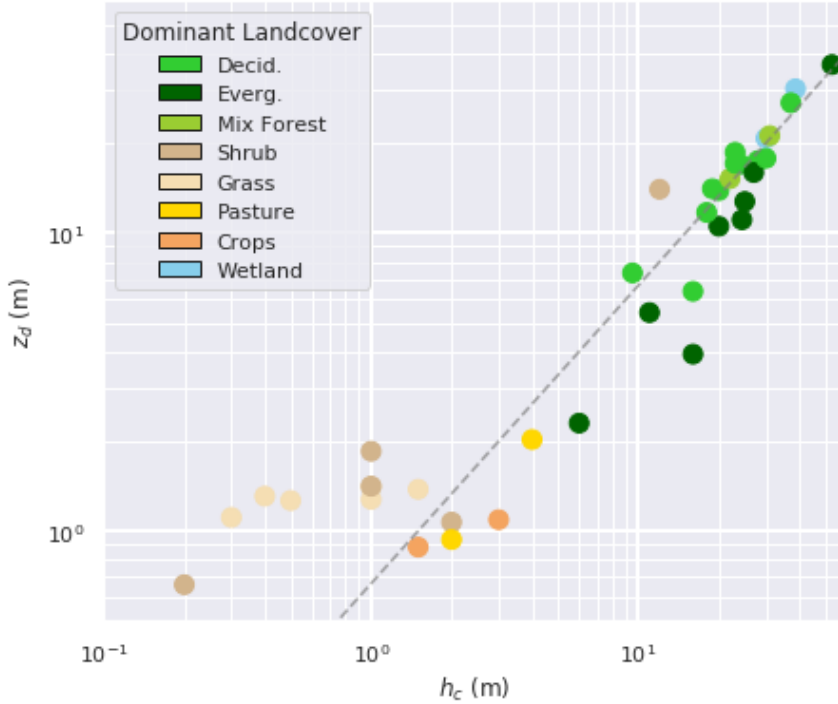


**Figure 2.** Comparison of reported canopy height ( $h_c$ ) and zero plane displacement height ( $z_d$ ). Colored according to the dominant land cover type at each site. Dotted line represents  $z_d = (2/3)h_c$  relations.

238

### 3.3 Quality Assurance and Quality Control

239

240

241

242

243

244

245

246

247

248

249

250

251

To ensure that the data are both of high quality and readily applicable, a number of quality assurance steps are applied: (1) All points that fail NEON quality assurance for air temperature are removed, (2) data where the reported energy balance has a residual greater than 20% are removed, as large residuals indicate high likelihood of significant advective fluxes and thus complicate the analysis (Mauder et al., 2020). The 20% threshold was selected to preserve as much data as possible for site-by-site analysis, and no significant difference in data quality or observed trends was noted when tightening this threshold further. (3) All data points with  $\zeta > 0$  are removed as uncertainties in this range are high, data availability is relatively low, and this is not the intended focus of the study. (4) Periods with non-negligible precipitation are removed. (5) Any site which, after all previous quality control is applied, retains less than 100 half-hourly runs are removed. Quality control retained just over 32,000 half-hourly runs across 39 NEON sites, roughly equivalent to about 2 site-years at 30-min averaging.

252

### 3.4 Random Forest (RF) Method

253

254

255

256

257

258

259

The RF method is used to generate an initial data-driven alternative model to equations 1 and 2 with no regards to dimensional constraints as required by similarity theory. This allows us to examine empirically impacts that various environmental predictors not present in current MOST based formulations might have on the development of PTV. The RF is a machine learning method that uses ensemble decision trees for producing a regression, with each decision tree run using a random subsample of the data to generate the model (Breiman, 2001). Data are split into testing and training datasets.

260 Accuracy is evaluated primarily using normalized root mean squared error (RMSE). From  
 261 the results of the model, we extract feature importance, a measure of which predictors  
 262 play the largest role in the model fit. In this case, high feature importance indicates that  
 263 the value of a given predictor is essential for describing and predicting PTV using the  
 264 RF method. We have elected to use sensible heat,  $\zeta$ , and  $u_*$  due to their role in MOST.  
 265 Tree cover fraction, bare soil fraction, vegetative fraction, LAI, and effective drag  $C_d =$   
 266  $[u_*/u(z)]^2$  are used to potentially represent canopy structure and roughness effects. BLH,  
 267 CAPE, and cloud cover fraction are selected due to their relation with mesoscale phe-  
 268 nomenon and large scale eddies.

## 269 4 Results

270 The analysis begins with basic examination of the data across all sites. These are  
 271 summarized as comparisons between  $\sigma_T$  and the environmental predictors presented in  
 272 section 3.4, followed by analysis of the diurnal cycle of sensible heat and  $\sigma_T$ . The data  
 273 are then compared to the curves of (1) and (2). Analysis continues focused on explor-  
 274 ing site level differences, first with RF over the entire dataset as well as individually for  
 275 each site. A bar plot showing the relation between predicted and observed at each site  
 276 is then featured to illustrate differences between land cover types. The final section of  
 277 the analysis focuses on evaluating potential model improvements leveraging the results  
 278 in the previous sections. The observations are compared to Equations 1 and 2 with up-  
 279 dated parameter values selected through curve fitting. This comparison is shown over  
 280 both the overall dataset and a select few sites. Finally, select parameterizations of the  
 281  $b$  parameter in (1) based on a variety of metrics that represent canopy structure are pre-  
 282 sented, evaluated, and compared to traditional formulations.

### 283 4.1 Holistic Exploration

284 The data from the remotely sensed products and NEON were merged and then qual-  
 285 ity controlled as described in section 3.3. Figure 3 presents a comparison between  $\sigma_T$  and  
 286 collocated environmental and meteorological data. The results show a clear relation be-  
 287 tween PTV and sensible heat flux  $H = \rho C_p \overline{w'\theta'}$  where  $\rho$  is the mean air density and  
 288  $C_p$  is the specific heat capacity of dry air at constant pressure as well as  $\zeta$  and to a lesser  
 289 extent effective drag  $C_d$ . In addition, some patterns seem apparent with LAI and BLH.  
 290 Other environmental variables not included in figure 3 have no significant relation with  
 291 PTV. For  $H$ , there appears to be a family of curves rather than one defined shape, im-  
 292 plying some additional parameter is influencing that relation. Effective drag, similarly,  
 293 has two families of curves, with the larger effective drag values arising primarily from  
 294 forested sites.

295 The diurnal cycles of PTV and  $H$  are plotted in figure 4. In the four forested sites,  
 296  $H$  is higher relative to  $\sigma_T$  when compared to the four low lying sites, already suggestive  
 297 of the importance of site level difference. Figure 4 is also illustrative of the differences  
 298 between unfiltered and filtered PTV, with the change being most significant in the morn-  
 299 ings when sensible heat flux is small but rapid changes in mean air temperature would  
 300 artificially inflate the apparent PTV caused by turbulence only.

301 The data covers a range of stability conditions in the near neutral and unstable range,  
 302 as indicated in figure 5a. The shape of the data generally follows expectations from MOST  
 303 with an extensive  $\zeta^{-1/3}$  scaling (Tillman, 1972) in figure 5b in the unstable range, al-  
 304 though in the near neutral range this is less clear. Similarly, in figure 5a, there is some  
 305 deviation from the established formulation in equation (1), especially as  $\zeta$  increases in  
 306 magnitude. Comparing equations (1) and (2) directly to the data show significant er-  
 307 rors. Equation (1) has an nRMSE of 21.5% and a 1% bias, although the bias in equa-  
 308 tion (1) is deceptive as the model has significant negative bias at low values and a pos-

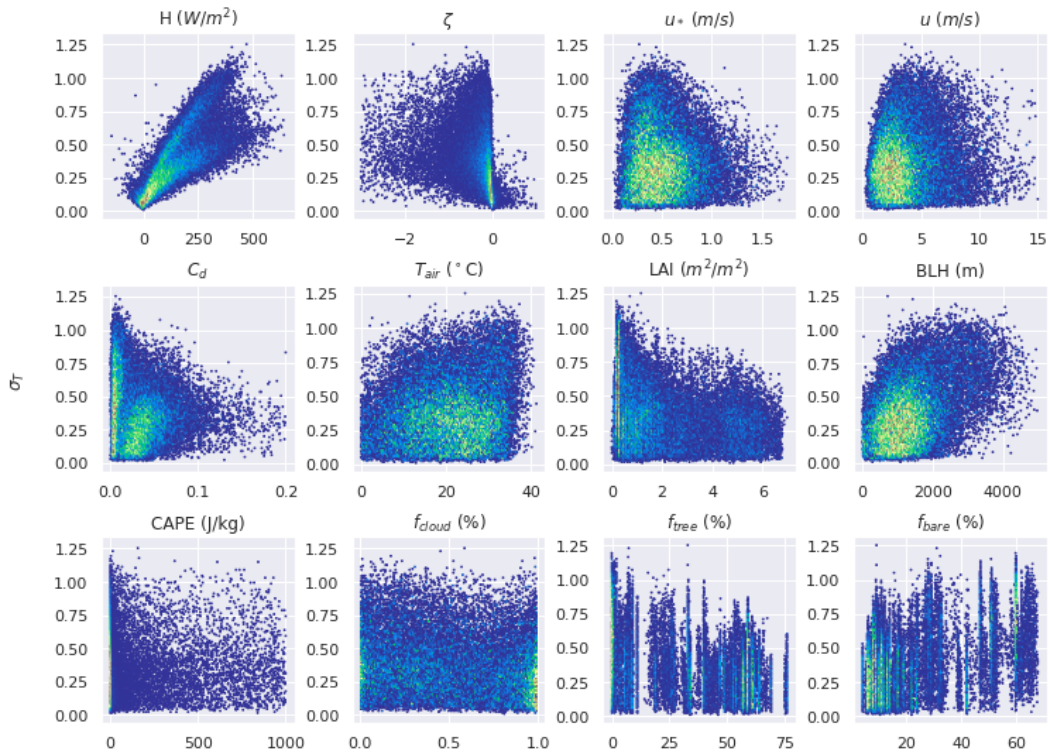


**Figure 3.** Relation between environmental variables and  $\sigma_T$  across all sites. The resulting scatterplots are binned into small hexagons; the colors illustrate the concentration of points in each hexagon where blue is low and yellow/brown is high.

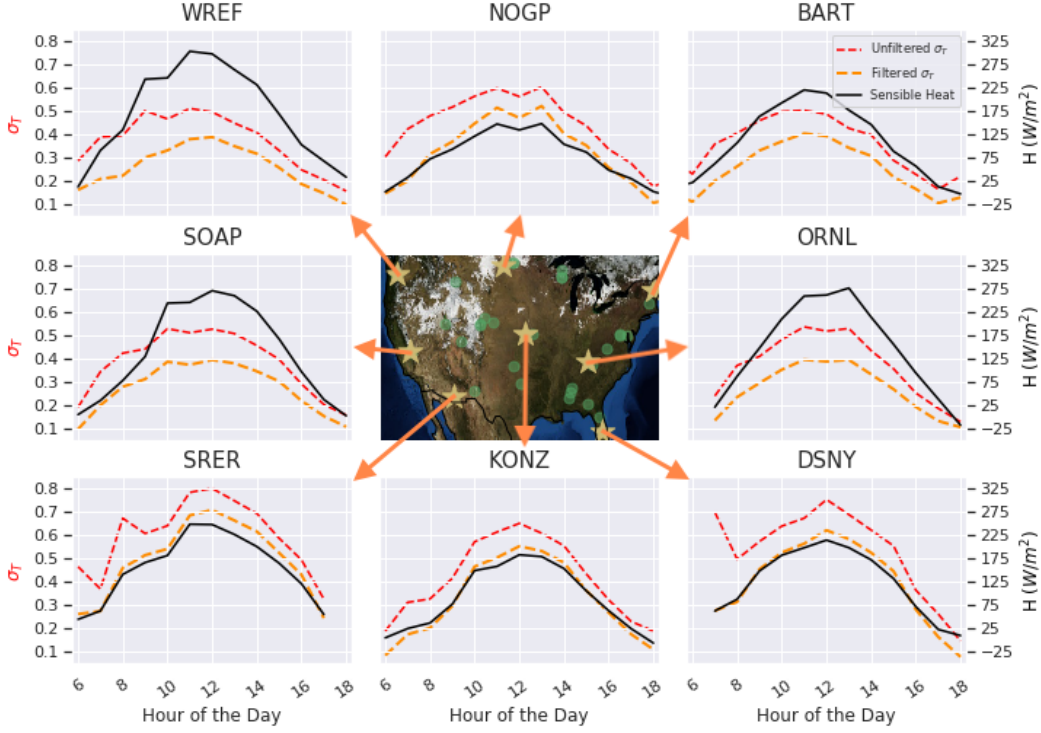


**Figure 4.** The diurnal cycle of sensible heat flux ( $H$ ), filtered (red-dashed) and unfiltered (orange-dashed)  $\sigma_T$  for 8 selected sites, with their locations indicated on the central map of CONUS.

309 itive bias at larger values. Equation (2) performs significantly worse over that range, with  
 310 an nRMSE of 27.6% and a bias of 15%.

311 **4.2 Site by Site Comparison**

312 Random Forest provides a first pass at the potential to improve upon the model  
 313 when noting deviations from the data in figure 5. RF does perform significantly better  
 314 than either model with nRMSE of 13.4% and a bias of less than 0.1%, although com-  
 315 putational constraints prevent its use in ESMs. The feature importance provides dynam-  
 316 ically interesting results as can be seen in figure 6. Sensible heat flux dominates the de-  
 317 termination of PTV as expected from flux variance literature. The relative unimportance  
 318 of friction velocity is also consistent with equation (2) and with equation (1) when the  
 319 magnitude of  $\zeta$  is large. The high importance of  $f_{tree}$  may be consistent with the results  
 320 in figure 4 as well, further indicating that tree cover has a significant impact on the re-  
 321 lation between sensible heat flux and PTV. Somewhat surprising is the relatively low im-  
 322 portance for  $\zeta$ . Although it is notable that since  $\zeta$  is a function of  $H$  and  $z_d$ , which is  
 323 related to canopy height, a significant portion of the stability effect may be captured by  
 324 these two aforementioned variables.

325 The results shown in figures 3, 4, and 6 all indicate the possibility of variable curves  
 326 for each site in the network. RF was run again, separately, for each individual site to ex-  
 327 amine these possible relations and remove any attempts by the algorithm to use a pre-  
 328 dictor as a proxy for the site. The violin plot in figure 6 shows the distribution of the  
 329 feature importance of each predictor across sites. When examined site by site,  $H$  is an  
 330 even more dominant predictor for PTV. The stability parameter becomes the second most

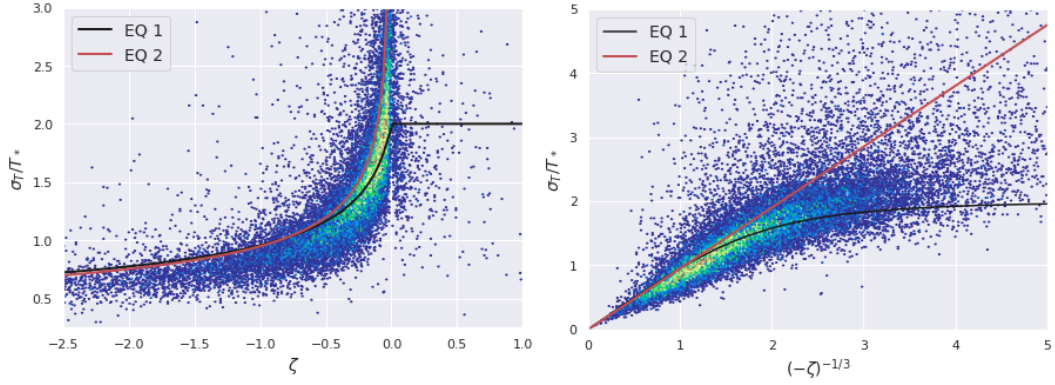


**Figure 5.** **a**(left): Relation between the dimensionless standard deviation of potential temperature  $\sigma_T/T_*$  and the stability parameter  $\zeta$  for the data with the modeled values from Equation (1) in black and Equation (2) in red. **b** (right): Relation between the dimensionless standard deviation of potential temperature and  $(-\zeta)^{-1/3}$ . The resulting scatterplots in both panels are binned into small hexagons; the colors illustrate the number of points in each hexagon where blue is low and yellow/brown is high.

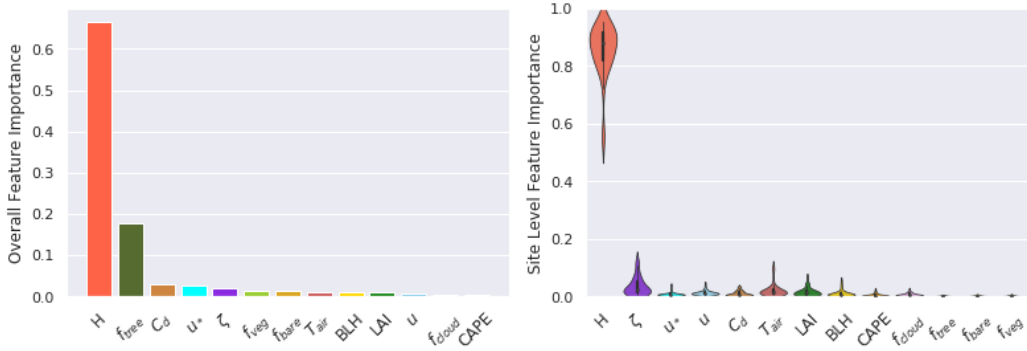


**Figure 6.** **a** (left): The feature importance from the random forest on the aggregate dataset sorted by overall importance. **b** (right): Results of the site level random forest feature importance. Violin plot shows distribution of site level feature importance for each predictor

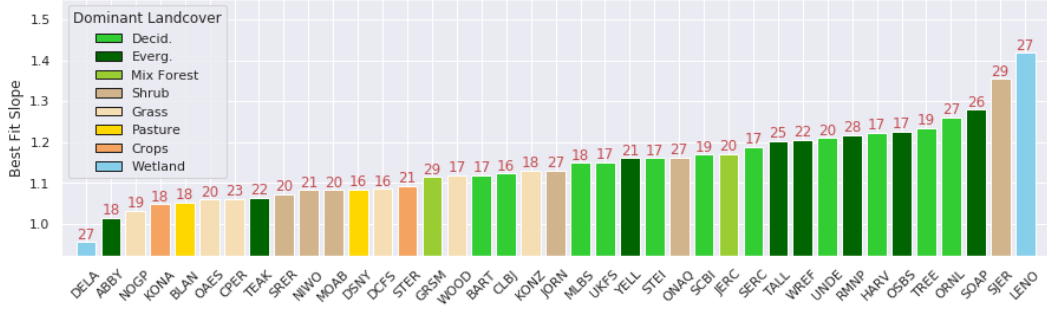


**Figure 7.** Bar plot showing the best fit slope between the observed and predicted temperature variance at each site using equation 1. Normalized RMSE is also listed in red above each bar. Site bars are colored by the dominant NLCD land cover

331 important indicator, consistent with preexisting MOST formulations, although again it  
 332 is small when compared to sensible heat flux.

333 When further exploring site level differences, key patterns begin to emerge. When  
 334 comparing the PTV predicted by equation 1 and the PTV observed at each site, there  
 335 is a significant variability in the slope of the best fit line of the data, which would ideally  
 336 sit at 1 indicating close agreement between the observations and the model. Figure  
 337 7 illustrates how that slope changes site to site and with land cover type. Sites with slopes  
 338 close to 1 are generally flat, homogeneous, and dominated by low lying vegetation, which  
 339 is the ideal landscape for MOST, and matches the landscapes where the values of the  
 340 parameters  $a$ ,  $b$  and  $C_1$  were originally derived. Forested sites however, especially those  
 341 with significant heterogeneities, have slopes significantly higher than 1, indicating that  
 342 the pre-existing model underpredicts PTV at low values and overpredicts PTV at high  
 343 values. LENO, SJER and SOAP in particular are all sparsely forested sites with significant  
 344 open water at LENO, an oak savannah at SJER, and sparse evergreens with varying  
 345 topography at SOAP. In addition, it is notable that ABBY is a logging site, so while  
 346 it is classified as evergreen, the actual canopy is quite short, and the tower is located in  
 347 a clearing.

### 348 4.3 Adjusting Existing Models

349 The results in figure (5) show that there is value in the existing schema and imply  
 350 that operational adjustments could yield improvements. An iterative fitting process  
 351 was used to determine the optimal values for the constants  $a$ ,  $b$ , and  $C_1$  over the aggregate  
 352 data. This global fit resulted in small but non-trivial model improvements for equation  
 353 (1) and equation (2) both in error and bias. Equation (1) after a global fit to the  
 354 data nRMSE changes from 20.5% to 17% while bias remains constant and for equation  
 355 (2) the error is reduced from 27.6% to 18.4% and bias shifts from 15% to -1.4%. Figure  
 356 8 illustrates how the newly fitted curves describe the entire data in two ways: dimensional  
 357 and dimensionless forms. The dimensional form of the comparison was selected  
 358 because it does not suffer from any self-correlation. Self correlation arises here because  
 359  $H$  impacts both  $T_*$  (ordinate) and  $\zeta$  (abscissa) in the MOST stability correction function,  
 360 which can lead to spurious agreement (especially in the exponent). In dimensional  
 361 form (left panels 8), the  $\sigma_T$  is computed from measured  $u_*$ ,  $H$ ,  $z$ , and inferred  $z_d$  and  
 362 compared to independently measured  $\sigma_T$  obtained after filtering the high frequency air  
 363 temperature series. Fitted equation (1) performs better than fitted equation (2) though  
 364 in dimensional form, this difference appears minor. This difference becomes clear when  
 365 the two formulations are assessed by stability class and appear to diverge in the near neu-

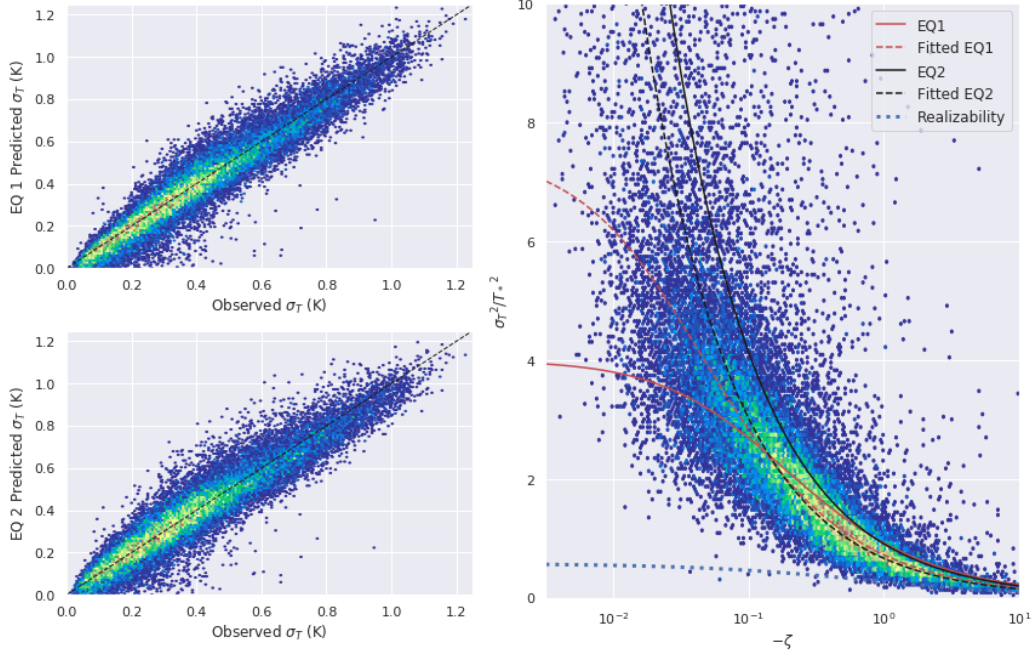


**Figure 8.** (upper left): Comparison between observed and predicted temperature variance by equation (1) after a global fit ( $a=7.5$ ,  $b=34.0$ ) over all sites. (bottom left): Comparison between observed and predicted temperature variance by equation (2) after a global fit ( $=.812$ ) over all sites. Note the comparisons in the left panels do not suffer from self-correlation. (right): the stability correction function for the non-dimensional temperature variance  $\sigma_T^2/T_*^2$ . The original forms of equation (1) ( $a=4$ ,  $b=8.3$ ) and equation (2) ( $=.95$ ) are shown as well as the fitted versions of both equations. In addition, the limit imposed by the realizability constraint is featured. The resulting scatterplots in all three are binned into small hexagons; the colors illustrate the number of points in each bin where blue is low and yellow/brown is high.

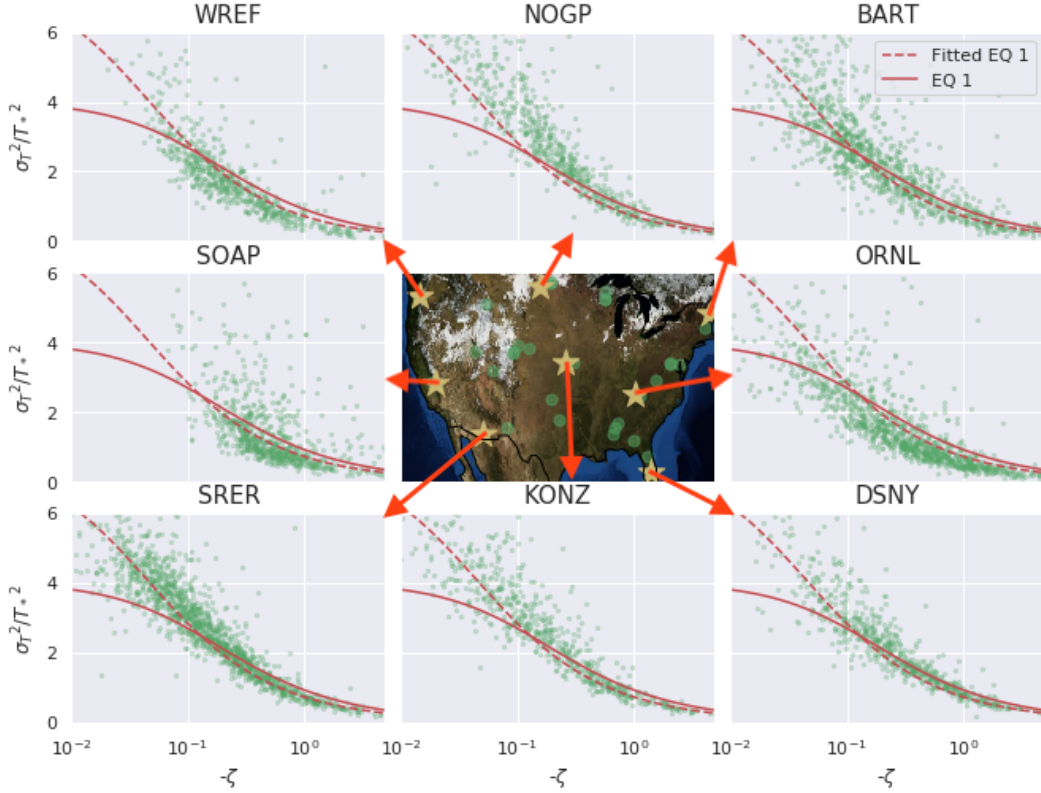


**Figure 9.** Stability correction function for the temperature variance at selected sites. In red, the modeled results are plotted for both the original Equation 1 ( $a=4$ ,  $b=8.3$ ) and the global fit Equation 1 ( $a=7.5$ ,  $b=34$ ) as well.

366 tral range. In this range, there is much greater uncertainty in the values of  $\sigma_T/T_*$  (though  
 367 the variances themselves are small). As  $T_* \rightarrow 0$  but  $\sigma_T$  remains finite due to entertain-  
 368 ment of heat and due to finite signal-to-noise ratio in the measurements,  $\sigma_T/T_*$  becomes  
 369 ill-defined or suspect in equation (1). Interestingly, equation (2) suggests that both the  
 370 left-hand and right-hand side becomes unbounded as  $T_* \rightarrow 0$ , and thus predicts rapid  
 371 increase in  $\sigma_T/T_*$  as  $|\zeta| \rightarrow 0$ . While this increase in  $\sigma_T/T_*$  appears to be consistent with  
 372 some data sets, it is simply a statement that  $\sigma_T/T_*$  may be ill-defined. As such, we will  
 373 be focusing our analysis on equation (1) in which  $\sigma_T/T_*$  is forced to approach a constant  
 374 and  $\sigma_T$  maintains its scaling with local sensible heat flux. Last, a realizability constraint  
 375 was also developed (described later) so as to illustrate a theoretical lower limit for the  
 376 applicability of equations (1) and (2). Figure 8 demonstrates that the majority of the  
 377 observations (in dimensionless form) as well as the changes in parameter values remain  
 378 above the line and satisfy this realizability constraint.

379 The global fit does not perform universally well at each site, although most sites  
 380 realize some improvements. Figure 9 shows the global fit and original equation (2) over  
 381 select sites as well as scatterplots of the data, similar to the hexbin scatterplot for the  
 382 aggregate data in figure 8c. At three of the sites, ORNL, WREF, and SOAP, the data  
 383 lies largely below both the original equation (1) curve as well as the fitted curve. These  
 384 sites all have significant forest cover, especially compared to the 4 sites where the data  
 385 lies largely above the fitted curve, NOGP, SRER, KONZ and DSNY, which are all flat  
 386 sites with only bare soil or low-lying vegetation.

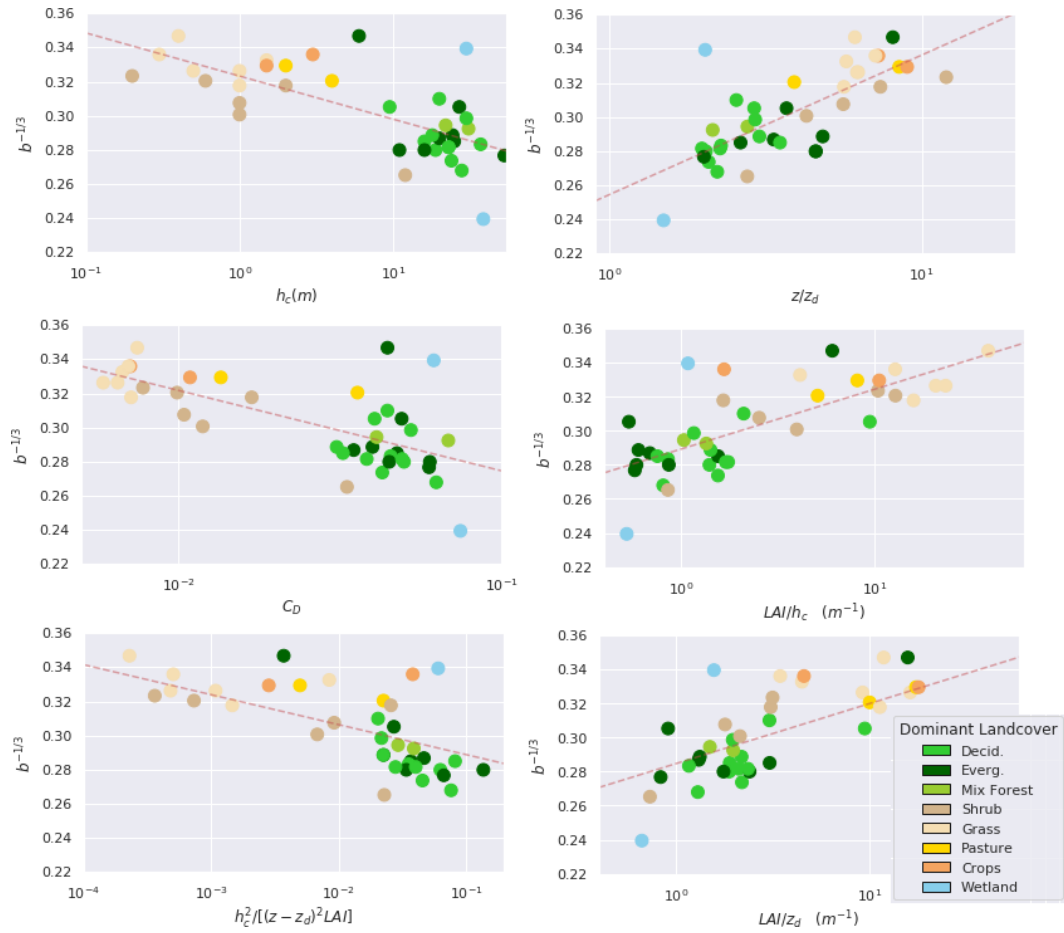


**Figure 10.** Scatterplot of the selected predictors at each site on a log scale compared to the best fit value for the  $b$  parameter for the MOST formulation. The points are colored according to the dominant NLCD landcover type

**Table 2.** Summary table of the results of various selections for the parameters of equations 1 and 2 as well as the random forest model. The table includes the normalized RMSEs and normalized biases of the different models for PTV.

<b>Equation 1</b>				
Model	$a$	$b$	nRMSE	nBias
Standard	4	8.3	20.5%	1.4%
Global Fit	7.5	34	17.0%	-2.7%
Site by Site Fit	7.5	varies	15.5%	-3.0%
<b>Equation 2</b>				
Model	$C_1$		nRMSE	nBias
Standard	0.95		27.6%	15%
Global Fit	0.812		18.4%	1.4%
<b>Random Forest</b>				
Model			nRMSE	nBias
Global	—		13.4%	< 0.1%

**Table 3.** Summary of a variety of possible parameterizations of the  $b$  parameter in equation (1) following the form of equation (6)

<b>Equation 8</b>					
$\chi$	$\alpha$	$\beta$	nRMSE	nBias	$R^2$
$LAI/h_c$	0.036	0.289	16.2%	-5.0%	0.55
$LAI/z_d$	0.036	0.284	16.3%	-4.8%	0.57
$z/z_d$	0.042	0.277	16.7%	-3.6%	0.54
$C_d$	-0.047	0.228	16.8%	-2.9%	0.46
$h_c^2/[(z - z_d)^2 LAI]$	-0.024	0.258	16.4%	-4.7%	0.52
$h_c$	-0.025	0.323	16.5%	-3.4%	0.5

387 These site level differences can also be examined more quantitatively. The fitting  
 388 exercise was repeated, this time doing a separate fit of the  $b$  parameter for each site while  
 389 holding  $a$  constant. The  $a$  is held constant and  $b$  is adjusted because under highly con-  
 390 vective conditions, which are the main conditions of interest,  $b$  is the dominant param-  
 391 eter whereas  $a$  dominates in the more uncertain near-neutral range. After comparing  $b$   
 392 and other environmental predictors, it became clear that there is a close relation between  
 393 a variety of measurements of canopy structure around the tower and the best fit value  
 394 of the  $b$  parameter. As shown in Figure 10, there is a clear linear relation between the  
 395 cube root of  $b$  and the different measurements of vegetative structure: canopy height,  
 396 leaf area density ( $LAI/h_c$ ), effective drag  $C_d$ ,  $z/z_d$ ,  $LAI/z_d$ , and  $h_c^2/[(z - z_d)^2 LAI]$ .

Taking advantage of this relation between  $b$  and the various proxies for canopy struc-  
 ture around the tower, a linear model was developed for  $b$  based on a linear regression.  
 Applying the model in Equation (6) to update the parameters in Equation (1) with the  
 existing data yields only marginal improvements on the updated Equation (1) based on  
 globally fit parameters, as is clear in Table 3. The relation

$$b^{-1/3} = \alpha \log(\chi) + \beta \tag{9}$$

397 does suggest that as canopy height increases,  $b$  also increases thereby amplifying the mod-  
 398 ulations introduced by  $\zeta$  that act to reduce the dimensionless temperature variance. Hence,  
 399 it appears that tall canopies make the dimensionless temperature variance more sensi-  
 400 tive to  $\zeta$ .

## 401 5 Discussion

### 402 5.1 Results Summary and Synthesis

403 Overall, the filtered data indicates agreement with the MOST based formulations  
 404 (Tillman, 1972). While this study emphasizes that there is room for improvement, it is  
 405 also important to note that equation (1) holds even over non-idealized landscapes and  
 406 conditions despite the fact that the formulation and parameter values were derived over  
 407 highly idealized flows. The evaluation of equation (1) over these wide-ranging landscapes  
 408 offers one of the clearest pictures in the literature of its broad applicability for under-  
 409 standing PTV at the bottom of the surface layer (provided non-turbulent phenomenon  
 410 are filtered). From the results of the random forest, and inspection of figure 2, it is ev-  
 411 ident that other local physical and meteorological characteristics that were thought to  
 412 have some influence on the development of PTV in the surface boundary are largely unim-  
 413 portant. Heat flux and local stability continue to be the driving factors and can yield  
 414 good predictions for PTV over flat landscapes using the standard parameter values. Based  
 415 on model error analysis, there is additional uncertainty to be captured.

416 Numerous studies have shown how parameter values for various local sites can devi-  
 417 ate from the global values described in the early literature, however few have proposed  
 418 updates to models used in ESMs as these studies often include only a very small num-  
 419 ber of sites and therefore painted a limited picture of the variety that one can find in the  
 420 field. Site by site fitting to the parameter values indicate that most sites have param-  
 421 eter values larger than those defined in the literature, and only one site was found to have  
 422 parameter values smaller. Since the best fit values of the parameters across landscapes  
 423 do not oscillate around these ‘ideal’ values, but rather are all greater than or equal to  
 424 them, ESMs can benefit from alternative global parameters to cover regions with var-  
 425 ied and heterogeneous canopies. The inter-site best fit parameter variation is quite sig-  
 426 nificant, with best fit values of  $b$  ranging from 20 to 80. This suggests that, while global  
 427 parameter values may be useful for broad application, localized studies will benefit most  
 428 from a local, site based empirical fit, especially if they deviate from ideal (i.e. flat, ho-  
 429 mogeneous, short vegetation) surfaces.

Attempts to use environmental predictors to capture the local variation were only  
 marginally successful outside of a random forest model. The RF method detailed sig-  
 nificant improvement, and was able to capture most of the inter-site variability based  
 on the tree cover fraction. This implies that canopy structure and surface roughness char-  
 acteristics are responsible for a significant portion of the deviations from ideal conditions.  
 The RF method, however, is too computationally intensive for application in ESMs. As  
 such, there was an attempt to generate a compact model for the  $b$  parameter based on  
 environmental variables related to surface roughness and canopy. Of a long list of pos-  
 sible predictors to model values of  $b$ , the most successful are shown in figure 10. A plu-  
 sibility argument for the inclusion of these variables used to parameterize  $b$  may be ob-  
 tained by examining the variance budget with the inclusion of the flux transport term.  
 In this case,

$$\overline{w'\theta'\theta'} = -D_{eff} \frac{\partial \overline{\theta'\theta'}}{\partial z}, \quad (10)$$

If this flux transport term is finite because of roughness sublayer effects, then  $D_{eff} \approx \sigma_w c_2 L_c$  where  $c_2 L_c$  are eddy sizes associated with canopy modifications based on the so-called adjustment length scale (Belcher et al., 2003). This adjustment length  $L_c = 1/(C_{d,c} a)$  where  $a = LAI/h_c$  is the mean leaf area density and  $C_{d,c}$  is a canopy drag coefficient

that differs from the local  $C_d$ . If so, then

$$0 = -2\overline{w'\theta'} \frac{\partial \overline{\theta}}{\partial z} + \frac{\partial}{\partial z} \left( \frac{c_2 \sigma_w h_c}{C_{d,c} LAI} \right) \frac{\partial \overline{\theta'\theta'}}{\partial z} - 2\epsilon_{\theta\theta}, \quad (11)$$

where  $\epsilon_{\theta\theta}$  is the temperature variance destruction term. To proceed further along the lines of dimensional analysis only, the flux transport term may be assumed to scale as

$$\frac{\partial}{\partial z} \left[ \frac{c_2 \sigma_w h_c}{C_{d,c} LAI} \frac{\partial \overline{\theta'\theta'}}{\partial z} \right] = - \frac{c_2 \sigma_w h_c}{C_{d,c} LAI} \frac{\overline{\theta'\theta'}}{(z - z_d)^2}, \quad (12)$$

whereas the  $\epsilon_{\theta\theta}$  is assumed to scale as

$$\epsilon_{\theta\theta} = \frac{1}{\tau} \frac{\overline{\theta'\theta'}}{C_{\epsilon,\theta}}, \quad (13)$$

and  $\tau$  is a relaxation time scale selected based on the ratio of turbulent kinetic energy and its mean dissipation rate, and  $C_{\epsilon,\theta}$  is a similarity constant. Thus, the variance budget becomes an algebraic expression of the form

$$-2 \frac{u_*}{k(z - z_d)} T_*^2 \phi_h(\zeta) + \overline{\theta'\theta'} \left[ \frac{c_2 \sigma_w h_c}{C_{d,c} LAI} \frac{1}{(z - z_d)^2} + \frac{1}{\tau} \frac{2}{C_{\epsilon,\theta}} \right] = 0, \quad (14)$$

where  $\phi_h$  is the flux-profile stability correction function. Hence,

$$\frac{\overline{\theta'\theta'}}{T_*^2} = 2\phi_h(\zeta) \frac{\frac{u_*}{k(z - z_d)}}{\frac{c_2 \sigma_w h_c}{C_{d,c} LAI} \frac{1}{(z - z_d)^2} + \frac{2}{\tau C_{\epsilon,\theta}}}, \quad (15)$$

430 thereby linking the flux-variance and the flux-profile stability correction functions. The  
 431 finding in equation 15 analysis qualitatively suggests that there are three time scales in-  
 432 volved: the classical shear time scale (congruent with MOST), a decorrelation time scale  
 433 (originating from the temperature variance destruction by molecular diffusion), and a  
 434 new ‘canopy’ distortion time scale originating from a communication between the rough-  
 435 ness sublayer and the atmospheric surface layer through a flux transport term. This find-  
 436 ing provides a plausibility argument for the relation between the canopy structure and  
 437 the  $b$  parameter seen in figure 10. While there is a clear relation between the various in-  
 438 terpretations of canopy structure and the value of the  $b$  parameter, none appear to have  
 439 strong predictive value. This could be due to the inherent variability of the data, improper  
 440 choice for the canopy structure proxy variable, or difficulties arising from the location  
 441 of the sensors.

442 In addition to deviations due to roughness effects, deviations from equation (1) due  
 443 to large scale eddies was also proposed as a source of uncertainty. The results paint an  
 444 unclear picture that neither confirms this hypothesis nor offers a clear refute. Figure 3  
 445 shows that there is a weak linear relation between BLH and the temperature variance,  
 446 suggesting that when the ABL is large, additional external sources of variance could ex-  
 447 ist, introducing new length scales not represented in MOST. The relation in Figure 3,  
 448 however, is weak. Figure 6a and 6b also support this weak relation. The three predic-  
 449 tors included in the RF to represent these effects, BLH, cloud cover fraction, and CAPE,  
 450 all have a feature importance of less than 1%. These three predictors, however, do have  
 451 their limitations and the weak relation shown here does not clearly refute the hypoth-  
 452 esis. The data comes from a reanalysis product with relatively poor resolution, mean-  
 453 ing that measurements of these values, particularly BLH are not necessarily reliable. An-  
 454 other important note is the specific selection of time periods where the surface energy  
 455 balance is largely closed. Previous literature indicates that sub-mesoscale circulations  
 456 may cause the non-closure of the surface energy balance (Mauder et al., 2020), which means  
 457 that by virtue of constraining the study to a closed energy balance we may be exclud-  
 458 ing the study periods where these circulations would have an impact. Likewise, the re-  
 459 moval of time scale longer than 5 min may also ameliorate sub-mesoscale circulation. Ad-  
 460 ditional studies, with more reliable and locally relevant measurements of BLH such as

461 through surface to air LIDAR as well as consideration of the surface energy balance, are  
 462 required to adequately assess this hypothesis.

It is also worth noting that all of the model adjustments presented in this paper, as well as the original Equations 1 and 2, satisfy the realizability constraint presented here. In this work, the realizability constraint requires that  $\theta'$  and  $w'$  must not be perfectly correlated resulting in the inequality

$$\sigma_w^2 \sigma_T^2 > (\overline{w'\theta'})^2 = (T_* u_*)^2 \quad (16)$$

and

$$\frac{\sigma_w^2 \sigma_T^2}{u_*^2 T_*^2} > 1 \quad (17)$$

Paired with the original formulation of equation (1) are equivalent MOST consistent forms for  $\sigma_w^2/u_*^2$  (Andre et al., 1978)

$$\frac{\sigma_w^2}{u_*^2} = 1.75 + 2(-\zeta)^{2/3} \quad (18)$$

Thus, combining equation (17) and equation (18) we obtain

$$\frac{\sigma_T^2}{T_*^2} > \frac{1}{\frac{\sigma_w^2}{u_*^2}} = \frac{1}{(1.75 + 2(-\zeta)^{2/3})} \quad (19)$$

463 Equation (19) is plotted as part of figure 8c, which clearly illustrates that the model  
 464 adjustments proposed do not violate any realizability constraint.

465 Another notable point of discussion is the role of the filtering exercise discussed in  
 466 section 3.1 in the accuracy of the fitted parameter values. Overall, the filtering process  
 467 yielded closer agreement to MOST; unfiltered data overall yields slightly more noise and  
 468 a greater deviation from traditional MOST relations with a larger magnitude of bias, but  
 469 maintains inter site trends with unfiltered data.

## 470 5.2 Challenges

471 Although the model updates defined here represent potential improvements, there  
 472 are caveats, outliers that fail to follow the trends, and additional considerations. The first  
 473 source of concern is the thickness of the roughness layer for heat. It is difficult to ensure  
 474 that the towers are reporting flow statistics outside of the roughness layer and in the in-  
 475 ertial layer, where MOST scaling is intended to apply. NEON towers are designed to lie  
 476 above the roughness layer (i.e. in the surface layer), and mean wind profiles at the sites  
 477 indicate that most sites are within the surface layer based on momentum considerations.  
 478 In addition, past studies have indicated that the thickness of the momentum roughness  
 479 layer and a roughness layer for scalar quantities such as potential temperature and wa-  
 480 ter vapor are not necessarily the same. For scalar quantities, the roughness layer can be  
 481 significantly thicker than those for momentum upon which the tower design is based (Raupach  
 482 & Thom, 1981). If points are indeed interrogated inside the scalar roughness sublayer,  
 483 this could yield significant changes in the values of temperature variance as the canopy  
 484 and surface elements play a greater role in introducing variable heat sources and sinks.  
 485 Related to this is a concern inherent in the design; towers over forested sites in NEON  
 486 are designed as a factor of the canopy height, but over low-lying vegetation it is defined  
 487 as simply a constant 8m. This means that the instrumentation may lie further up in a  
 488 normalized profile for some of the flatter sites than the forested ones, potentially explain-  
 489 ing some of the differences between these two categories. Initial exploration does show  
 490 a poor but persistent relation between the ratio of tower height to canopy height and  
 491 the model parameter values. These challenges with defining where the instrumentation  
 492 lies above the canopy, however, is of lesser concern for the primary intended application

493 of this study in earth system models, where the roughness layer is inconsistently defined  
494 across different models.

495 When examining figures 6 and 9, a few sites seem to defy trends that have been  
496 discussed in this paper. These sites are relatively unique and illustrate probable sources  
497 for some of the additional uncertainty and errors. The three sites with the largest best  
498 fit slopes, and therefore the greatest deviation from the original Equation 1, are LENO,  
499 SOAP and SJER. All of these sites have sparse canopy and high spatial heterogeneity.  
500 Sparse canopy, such as those found at these sites, certainly deviate significantly from the  
501 MOST ideal and literature indicates that turbulent eddies formed over such canopies due  
502 to element wake diffusion effect among others could augment vertical diffusion of scalar  
503 quantities such as temperature and increase the observed variance, providing a possible  
504 rationale for these deviations (Raupach & Thom, 1981; Mironov & Sullivan, 2010). More  
505 work exploring this phenomenon over sparse canopies is required.

### 506 **5.3 Future Work**

507 A robust evaluation of the primary models of PTV at the surface layer was under-  
508 taken and avenues for improvements proposed. In addition to the importance of refin-  
509 ing models over sparse canopies, as discussed in the previous section, exploration of these  
510 models and PTV more generally in stable and, to a lesser extent, near neutral atmospheric  
511 regimes is needed. The model currently assumes that the non-dimensional variance re-  
512 mains constant with stability, although when exploring the data this became less clear.  
513 Previous studies have suggested high errors in the near neutral range is a consequence  
514 of the non-stationarity (Kroon & de Bruin, 1995; J. Wyngaard & Coté, 1971). This ef-  
515 fect may be partly ameliorated by spectral filtering as shown. Yet, the data scatter at  
516 the near neutral limit is undisputed. Significant scatter also exists in the mildly unsta-  
517 ble range, implying that there are issues with the application of MOST under these con-  
518 ditions that require more work.

519 There are three other avenues of future research that require further exploration.  
520 First, while this study focused on the case where the energy balance is closed and there  
521 is no significant advection, unbalanced conditions where sensible heat, latent heat and  
522 ground heat flux fail to account for the energy balance constitute a large fraction of the  
523 data. Initial work shows a clear shift in the fit of the data to Equation 1 under these con-  
524 ditions, with lower best fit parameter values and larger scatter. Unfortunately, explor-  
525 ing the potential effect of significant advection require model simulations or data not avail-  
526 able through NEON. The second avenue of future research is examining the analogous  
527 models for the other primary atmospheric scalar, water vapor. The model assumes that  
528 temperature and moisture behave similarly, with the same parameter values. Numerous  
529 studies, as well as initial examination of the NEON data, illustrate that water vapor and  
530 temperature do not behave identically (G. G. Katul & Hsieh, 1999; Asanuma & Brut-  
531 saert, 1999) in the surface layer as previously theorized, and as such an alternative model,  
532 or at the very least, alternative values for the  $a$  and  $b$  parameters are needed. Finally,  
533 results and previous literature have indicated that surface heterogeneity can have a sig-  
534 nificant impact on MOST derived parameterizations such as the ones discussed here. A  
535 brief examination, not presented here, implies there is a complex relation between het-  
536 erogeneity and temperature variance statistics and as such additional work considering  
537 different length scales of surface heterogeneity may indicate new directions for improve-  
538 ment and model analysis.

## 539 **6 Conclusion**

540 High frequency time series across 39 similarly instrumented sites covering varied  
541 landscapes across CONUS were analyzed to assess the validity of existing models for tem-  
542 perature variance in the surface layer, note key deficiencies and recommend avenues for

543 improvement. Results indicated that conventional flux-variance similarity formulations  
 544 are largely corroborated by data in both dynamic-convective and nearly convective cases  
 545 provided non-turbulent features are spectrally filtered out. This filtering reduced the tem-  
 546 perature variance by factors of 2 to 3 in some cases when compared to the unfiltered runs.  
 547 The most significant deviations from standard MOST formulations were observed over  
 548 heterogeneous and forested sites. Site by site analysis also revealed bias towards simi-  
 549 larity constants larger than the traditional parameter values used in the literature and  
 550 ESMs. A random forest model illustrated that there is variability not captured by the  
 551 traditional formulations. Results generally indicate that canopy structure, surface het-  
 552 erogeneity, and roughness characteristics drive a portion of the inter-site variability, al-  
 553 though a dimensional approach was unable to illustrate superior predictive value. Fu-  
 554 ture studies will expand this analysis to include situations with non-local energy balance  
 555 closure as well as landscapes with sparse canopies or large surface heterogeneities. Wa-  
 556 ter vapor and carbon dioxide concentration, the other primary atmospheric scalars, use  
 557 the same formulation in CLUBB and other models as PTV, although the literature shows  
 558 a difference in behavior. As such, any updated parameter values for temperature can-  
 559 not be applied to other scalars and additional work is required to make similar improve-  
 560 ments to their variance fluctuations.

## 561 Acknowledgments

562 This research has been supported by the National Oceanic and Atmospheric Adminis-  
 563 tration, Climate Program Office grant nos. NA19OAR4310241

564 The ERA 5 Reanalysis data (doi:10.24381/cds.adbb2d47) was downloaded from the  
 565 Copernicus Climate Change Service (C3S) Climate Data Store. The results contain mod-  
 566 ified Copernicus Climate Change Service information 2020. Neither the European Com-  
 567 mission nor ECMWF is responsible for any use that may be made of the Copernicus in-  
 568 formation or data it contains. MODIS Vegetative cover data (doi:10.5067/MODIS/MOD44B.006)  
 569 and Leaf Area Index (doi:10.5067/MODIS/MCD15A2H.006) is available through <https://lpdaac.usgs.gov/>.  
 570 NEON turbulence data is available through <https://data.neonscience.org/data-products/DP4.00200.001>  
 571 (doi:10.48443/bway-hc74). Finally, Land Cover types (2016 Version) from the National  
 572 Land Cover Database are available from the Multi-Resolution Land Characteristics Con-  
 573 sortium database <https://www.mrlc.gov/data>. Software used to process this data and  
 574 generate results can be found here: <https://tinyurl.com/tswneon>.

## 575 References

- 576 Albertson, J. D., Parlange, M. B., Katul, G. G., Chu, C., Stricker, H., & Tyler,  
 577 S. (1995). Sensible Heat Flux From Arid Regions: A Simple Flux-  
 578 Variance Method. *Water Resources Research*, *31*(4), 969–973. doi:  
 579 10.1029/94WR02978
- 580 Andre, J., De Moor, G., Lacarrere, P., Therry, G., & Du Vachat, R. (1978). Model-  
 581 ing the 24hr Evolution of the Mean and Turbulent Structures of the Planetary  
 582 Boundary Layer. *Direction de la Meteorologie*, *35*, 1861–1883.
- 583 Antonia, R. A., Chambers, A. J., & Bradley, E. F. (1981). Temperature Structure in  
 584 the Atmospheric Surface Layer. *Boundary-Layer Meteorology*, *20*, 293–307.
- 585 Asanuma, J., & Brutsaert, W. (1999). Turbulence variance statistics of Tem-  
 586 perature and humidity in the unstable atmospheric surface layer above a  
 587 variable pine forest. *Water Resources Research*, *35*(2), 515–521. doi:  
 588 10.1029/1998WR900051
- 589 Belcher, S. E., Jerram, N., & Hunt, J. C. (2003). Adjustment of a turbulent bound-  
 590 ary layer to a canopy of roughness elements. *Journal of Fluid Mechanics*, *488*,  
 591 369–398. doi: 10.1017/S0022112003005019
- 592 Breiman, L. (2001). Random Forests. *Machine Learning*, *45*, 5–32. doi: doi.org/10  
 593 .1023/A:1010933404324

- 594 Brunet, Y. (2020). Turbulent Flow in Plant Canopies: Historical Perspective and  
 595 Overview. *Boundary-Layer Meteorology*, *177*, 315–364. doi: 10.1007/s10546  
 596 -020-00560-7
- 597 Champagne, F. H., Friehe, C. A., LaRue, J. C., & Wyngaard, J. (1977). Flux  
 598 Measurements, Flux Estimation Techniques, and Fine-Scale Turbulence  
 599 Measurements in the Unstable Surface Layer Over Land. *Journal of Atmo-*  
 600 *spheric Sciences*, *34*(3), 515-530. doi: 10.1175/1520-0469(1977)034<0515:  
 601 FMFETA>2.0.CO;2
- 602 Cheng, A., & Xu, K. M. (2015). Improved low-cloud simulation from the community  
 603 atmosphere model with an advanced third-order turbulence closure. *Journal of*  
 604 *Climate*, *28*(14), 5737–5762. doi: 10.1175/JCLI-D-14-00776.1
- 605 Cohen, A. E., Cavallo, S. M., Coniglio, M. C., & Brooks, H. E. (2015). A review  
 606 of planetary boundary layer parameterization schemes and their sensitivity  
 607 in simulating southeastern U.S. cold season severe weather environments.  
 608 *Weather and Forecasting*, *30*(3), 591–612. doi: 10.1175/WAF-D-14-00105.1
- 609 Detto, M., Katul, G., Mancini, M., Montaldo, N., & Albertson, J. D. (2008).  
 610 Surface heterogeneity and its signature in higher-order scalar similarity re-  
 611 lationships. *Agricultural and Forest Meteorology*, *148*(6-7), 902–916. doi:  
 612 10.1016/j.agrformet.2007.12.008
- 613 DiMiceli, C., Carroll, M., Sohlberg, R., Kim, D., Kelly, M., & Townshend, J. (2015).  
 614 *Mod44b modis/terra vegetation continuous fields yearly l3 global 250m sin*  
 615 *grid v006*. NASA EOSDIS Land Processes DAAC. doi: 10.5067/MODIS/  
 616 MOD44B.006
- 617 Foken, T. (2006). 50 years of the Monin-Obukhov similarity theory. *Boundary-Layer*  
 618 *Meteorology*, *119*(3), 431–447. doi: 10.1007/s10546-006-9048-6
- 619 Garratt, J. R. (1992). *The Atmospheric Boundary Layer*. Cambridge University  
 620 Press.
- 621 Golaz, J. C., Caldwell, P. M., Van Roekel, L. P., Petersen, M. R., Tang, Q., Wolfe,  
 622 J. D., ... Zhu, Q. (2019). The DOE E3SM Coupled Model Version 1:  
 623 Overview and Evaluation at Standard Resolution. *Journal of Advances in*  
 624 *Modeling Earth Systems*, *11*(7), 2089–2129. doi: 10.1029/2018MS001603
- 625 Golaz, J. C., Larson, V. E., & Cotton, W. R. (2002). A PDF-based model for  
 626 boundary layer clouds. Part I: Method and model description. *Journal of*  
 627 *the Atmospheric Sciences*, *59*(24), 3540–3551. doi: 10.1175/1520-0469(2002)  
 628 059(3540:APBMFB)2.0.CO;2
- 629 Hang, C., Nadeau, D. F., Pardyjak, E. R., & Parlange, M. B. (2018). A comparison  
 630 of near-surface potential temperature variance budgets for unstable atmo-  
 631 spheric flows with contrasting vegetation cover flat surfaces and a gentle slope.  
 632 *Environmental Fluid Mechanics*, *20*. doi: 10.1007/s10652-018-9647-z
- 633 Harman, I. N. (2012). The Role of Roughness Sublayer Dynamics Within Surface Ex-  
 634 change Schemes. *Boundary-Layer Meteorology*, *142*(1), 1–20. doi: 10.1007/  
 635 s10546-011-9651-z
- 636 Haugen, D. A., Kaimal, J. C., & Bradley, E. F. (1971). An experimental study  
 637 of Reynolds stress and heat flux in the atmospheric surface layer. *Quar-*  
 638 *terly Journal of the Royal Meteorological Society*, *97*(412), 168–180. doi:  
 639 10.1002/qj.49709741204
- 640 Hersbach, H., Bell, B., Berrisford, P., Biavati, G., Horányi, A., Muñoz Sabater, J.,  
 641 ... Thépaut, J.-N. (2018). *Era5 hourly data on single levels from 1979 to*  
 642 *present*. Copernicus Climate Change Service (C3S) Climate Data Store (CDS).  
 643 doi: 10.24381/cds.adbb2d47
- 644 Huang, H. Y., & Margulis, S. A. (2010). Evaluation of a fully coupled large-eddy  
 645 simulation-land surface model and its diagnosis of land-atmosphere feedbacks.  
 646 *Water Resources Research*, *46*(6), 1–19. doi: 10.1029/2009WR008232
- 647 Jin, S., Homer, C., Yang, L., Danielson, P., Dewitz, J., Li, C., ... Howard, D.  
 648 (2019). Overall methodology design for the united states national land cover

- 649 database 2016 products. *Remote Sensing*, 11(24). doi: 10.3390/rs11242971
- 650 Kader, B. A., & Yaglom, A. M. (1990). Mean fields and fluctuation moments in  
651 unstably stratified turbulent boundary layers. *Journal of Fluid Mechanics*,  
652 212(151), 637–662. doi: 10.1017/S0022112090002129
- 653 Katul, G., Goltz, S. M., Hsieh, C. I., Cheng, Y., Mowry, F., & Sigmon, J. (1995).  
654 Estimation of surface heat and momentum fluxes using the flux-variance  
655 method above uniform and non-uniform terrain. *Boundary-Layer Meteorol-*  
656 *ogy*, 74(3), 237–260. doi: 10.1007/BF00712120
- 657 Katul, G. G., & Hsieh, C.-i. (1999). A note on the flux-variance similarity rela-  
658 tionships for heat and water vapour in the unstable atmospheric surface layer.  
659 *Boundary-Layer Meteorology*, 90(2), 327–338.
- 660 Kiely, G., Albertson, J. D., Parlange, M. B., & Eichinger, W. E. (1996). Convective  
661 scaling of the average dissipation rate of temperature variance in the atmo-  
662 spheric surface layer. *Boundary-Layer Meteorology*, 77(3-4), 267–284. doi:  
663 10.1007/BF00123528
- 664 Kroon, L. J., & de Bruin, H. A. (1995). The Crau field experiment: turbulent ex-  
665 change in the surface layer under conditions of strong local advection. *Journal*  
666 *of Hydrology*, 166(3-4), 327–351. doi: 10.1016/0022-1694(94)05092-C
- 667 Larson, V. E. (2017). *CLUBB-SILHS: A parameterization of subgrid variability in*  
668 *the atmosphere*. Retrieved from <http://arxiv.org/abs/1711.03675>
- 669 Lee, Y. H. (2009). The influence of local stability on heat and momentum transfer  
670 within open canopies. *Boundary-Layer Meteorology*, 132(3), 383–399. doi: 10  
671 .1007/s10546-009-9405-3
- 672 Li, D., Katul, G. G., & Gentine, P. (2016). The k-1 scaling of air temperature spec-  
673 tra in atmospheric surface layer flows. *Quarterly Journal of the Royal Meteorolo-*  
674 *gical Society*, 142(694), 496–505. doi: 10.1002/qj.2668
- 675 Li, Q., Gentine, P., Mellado, J. P., & Mccoll, K. A. (2018). Implications of nonlocal  
676 transport and conditionally averaged statistics on Monin-Obukhov similarity  
677 theory and Townsend’s attached eddy hypothesis. *Journal of the Atmospheric*  
678 *Sciences*, 75(10), 3403–3431. doi: 10.1175/JAS-D-17-0301.1
- 679 Lloyd, C. R., Culf, A. D., Dolman, A. J., & Gash, J. H. (1991). Estimates of sen-  
680 sible heat flux from observations of temperature fluctuations. *Boundary-Layer*  
681 *Meteorology*, 57(4), 311–322. doi: 10.1007/BF00120051
- 682 Lock, A. P., Martin, G. M., Bush, M. R., Brown, A. R., & Smith, R. N. (2000). A  
683 new boundary layer mixing scheme part II: Tests in climate and mesoscale  
684 models. *Monthly Weather Review*, 128(9), 3200–3217. doi: 10.1175/  
685 1520-0493(2000)128(3200:ANBLMS)2.0.CO;2
- 686 Maronga, B., & Reuder, J. (2017). On the formulation and universality of Monin-  
687 Obukhov similarity functions for mean gradients and standard deviations in  
688 the unstable surface layer: Results from surface-layer-resolving large-eddy  
689 simulations. *Journal of the Atmospheric Sciences*, 74(4), 989–1010. doi:  
690 10.1175/JAS-D-16-0186.1
- 691 Mauder, M., Foken, T., & Cuxart, J. (2020). *Surface-Energy-Balance Closure over*  
692 *Land: A Review* (Vol. 177) (No. 2-3). doi: 10.1007/s10546-020-00529-6
- 693 Mcnaughton, K. G. (2006). On the kinetic energy budget of the unstable atmo-  
694 spheric surface layer. *Boundary-Layer Meteorology*, 118(1), 83–107. doi: 10  
695 .1007/s10546-005-3779-7
- 696 Metzger, S., Ayres, E., Durden, D., Florian, C., Lee, R., Lunch, C., . . . Zulueta,  
697 R. C. (2019). From neon field sites to data portal: A community resource for  
698 surface-atmosphere research comes online. *Bulletin of the American Meteorolo-*  
699 *gical Society*, 100(11), 2305–2325. doi: 10.1175/BAMS-D-17-0307.1
- 700 Mironov, D. V., & Sullivan, P. P. (2010). Effect of horizontal surface tempera-  
701 ture heterogeneity on turbulent mixing in the stably stratified atmospheric  
702 boundary layer. Paper presented at 19th Symposium on Boundary Layers and  
703 Turbulence, American Meteorological Society, Keystone, Colorado.

- 704 Mironov, D. V., & Sullivan, P. P. (2016). Second-moment budgets and mixing  
 705 intensity in the stably stratified atmospheric boundary layer over thermally  
 706 heterogeneous surfaces. *Journal of the Atmospheric Sciences*, *73*(1), 449–464.  
 707 doi: 10.1175/JAS-D-15-0075.1
- 708 Monin, A. S., & Obukhov, A. M. (1954). Basic Laws of Turbulent mixing in the  
 709 surface layer of the atmosphere. *Tr. Akad. Nauk SSSR Geophys. Inst.*, *24*(151),  
 710 163–187.
- 711 Monji, N. (1973). Budgets of Turbulent Energy and Temperature Variance in  
 712 the Transition Zone from Forced to Free Convection. *J. Meteor. Soc. Japan*,  
 713 *51* (April), 133–145.
- 714 Myneni, R., Park, T., & Knyazikhin, Y. (2015). *Mcd15a2h modis/terra+aqua leaf*  
 715 *area index/fpar 8-day l4 global 500m sin grid v006*. NASA EOSDIS Land Pro-  
 716 cesses DAAC. doi: 10.5067/MODIS/MCD15A2H.006
- 717 Nakanishi, M., & Niino, H. (2009). Development of an improved turbulence closure  
 718 model for the atmospheric boundary layer. *Journal of the Meteorological Soci-*  
 719 *ety of Japan*, *87*(5), 895–912. doi: 10.2151/jmsj.87.895
- 720 National Ecological Observatory Network (NEON). (2021). *Bundled data products*  
 721 *- eddy covariance (dp4.00200.001)*. National Ecological Observatory Network  
 722 (NEON). Retrieved from [https://data.neonscience.org/data-products/](https://data.neonscience.org/data-products/DP4.00200.001/RELEASE-2021)  
 723 [DP4.00200.001/RELEASE-2021](https://data.neonscience.org/data-products/DP4.00200.001/RELEASE-2021) doi: 10.48443/BWAY-HC74
- 724 Novick, K. A., Biederman, J. A., Desai, A. R., Litvak, M. E., Moore, D. J., Scott,  
 725 R. L., & Torn, M. S. (2018). The AmeriFlux network: A coalition of the will-  
 726 ing. *Agricultural and Forest Meteorology*, *249*(October 2017), 444–456. doi:  
 727 10.1016/j.agrformet.2017.10.009
- 728 Obukhov, A. M. (1946). 'Turbulentnost' v temperaturnoj – neodnorodnoj atmosfere  
 729 (turbu- lence in an atmosphere with a non-uniform temperature). *Trudy Inst.*  
 730 *Theor. Geofiz. AN SSSR*, *1*, 95–115.
- 731 Oke, T. R. (1987). *Boundary layer climates*. Psychology Press.
- 732 Otić, I., Grötzbach, G., & Wörner, M. (2005). Analysis and modelling of the  
 733 temperature variance equation in turbulent natural convection for low-  
 734 Prandtl-number fluids. *Journal of Fluid Mechanics*, *525*, 237–261. doi:  
 735 10.1017/S0022112004002733
- 736 Poggi, D., Porporato, A., Ridolfi, L., Albertson, J., & Katul, G. (2004). The effect of  
 737 vegetation density on canopy sub-layer turbulence. *Boundary-Layer Meteorol-*  
 738 *ogy*, *111*(3), 565–587.
- 739 Raupach, M. R., Finnigan, J. J., & Brunet, Y. (1996). Coherent eddies and turbu-  
 740 lence in vegetation canopies: the mixing-layer analogy. *Boundary-Layer Meeo-*  
 741 *rology*, *78*(3-4), 351–382. doi: 10.1007/BF00120941
- 742 Raupach, M. R., & Thom, A. S. (1981). Turbulence in and above plant canopies.  
 743 *Annual review of fluid mechanics*, *3*, 97–129.
- 744 Siqueira, M., Katul, G., & Porporato, A. (2009). Soil moisture feedbacks on convec-  
 745 tion triggers: The role of soil-plant hydrodynamics. *Journal of Hydrometeorol-*  
 746 *ogy*, *10*(1), 96–112. doi: 10.1175/2008JHM1027.1
- 747 Tillman, J. (1972). The Indirect Determination of Stability, Heat and Momentum  
 748 Fluxes in the Atmospheric Boundary Layer from Simple Scalar Variables Dur-  
 749 ing Dry Unstable Conditions. *Journal of Applied Meteorology and Climatology*,  
 750 *11*(5), 1–27. doi: 10.1175/1520-0450(1972)011<0783:TIDOSH>2.0.CO;2
- 751 van de Boer, A., Moene, A. F., Graf, A., Schüttemeyer, D., & Simmer, C. (2014).  
 752 Detection of Entrainment Influences on Surface-Layer Measurements and Ex-  
 753 tension of Monin-Obukhov Similarity Theory. *Boundary-Layer Meteorology*,  
 754 *152*(1), 19–44. doi: 10.1007/s10546-014-9920-8
- 755 Wilson, J. D. (2008). Monin-Obukhov functions for standard deviations of veloc-  
 756 ity. *Boundary-Layer Meteorology*, *129*(3), 353–369. doi: 10.1007/s10546-008  
 757 -9319-5
- 758 Wyngaard, J., & Coté, O. (1971). Local Free Convection, Stability, and Budget

- 759 of Shear Stress and Heat Flux. *Journal of Atmospheric Sciences*, 28(7), 1–27.  
760 doi: 10.1175/1520-0469(1971)028<1171:LFCSAT>2.0.CO;2
- 761 Wyngaard, J. C., & Côté, O. R. (1974). The evolution of a convective planetary  
762 boundary layer - A higher-order-closure model study. *Boundary-Layer Meteorology*, 7(3), 289–308. doi: 10.1007/BF00240833
- 763
- 764 Zhao, M., Golaz, J. C., Held, I. M., Guo, H., Balaji, V., Benson, R., ... Xiang, B.  
765 (2018). The GFDL Global Atmosphere and Land Model AM4.0/LM4.0:  
766 2. Model Description, Sensitivity Studies, and Tuning Strategies. *Journal of Advances in Modeling Earth Systems*, 10(3), 735–769. doi: 10.1002/  
767 2017MS001209  
768